Journal of Applied Mathematics and Computational Mechanics 2026, 25(2), 28-39
www.amcm.pcz.pl p-ISSN 2299-9965
DOI: 10.17512/jamcm.2026.2.02 e-ISSN 2353-0588

NUMERICAL ANALYSIS OF A COUPLED DIFFUSION-SOLIDIFICATION MODEL WITH PHASE-DEPENDENT MATERIAL PROPERTIES

***Ewa Węgrzyn-Skrzypczak*[1], *Tomasz Skrzypczak*[2]**

[1] Department of Mathematics, Czestochowa University of Technology
Częstochowa, Poland
[2] Department of Mechanics and Fundamentals of Machine Design
Czestochowa University of Technology
Częstochowa, Poland
ewa.wegrzyn-skrzypczak@pcz.pl, tomasz.skrzypczak@pcz.pl

Received: 2 January 2026; Accepted: 30 March 2026

Abstract. This study focuses on the numerical modeling of a solidification process where solute transport is mainly controlled by diffusion. The problem is solved using the finite element method. The model describes the time evolution of temperature, phase fraction, and solute mass fraction in the liquid phase. Material properties are allowed to change locally depending on the phase state. Convective effects are not included. This is done on purpose, so that diffusive transport can be studied without additional flow-related effects. Latent heat is introduced using an effective heat capacity approach. Solute redistribution is described by a source term linked to the phase change. The simulation is performed in a time-dependent framework. After the calculations, the total amount of solute in the phase mixture is evaluated. Its global balance is monitored during the simulations to check mass conservation. The results show clear patterns of solute accumulation that are typical for diffusion-dominated solidification.

MSC 2010: *65M60, 68U20*
Keywords: *numerical modeling, finite element method, diffusion-dominated transport, solidification, phase-change problems*

1. Introduction

Solidification is often studied using numerical models. These models usually include heat transfer, phase change, and solute transport. They are widely used in materials processing, where experiments are hard or expensive to perform. Many studies show that temperature changes in time are important for real processes. One example is the work of Suliga et al. [1]. They used both simulations and experiments to study temperature during high-speed drawing of steel wires. Their results show that transient heat transfer and changing material properties have a strong effect on the process.

In solidification of metals, temperature is not the only important factor. The final distribution of solute also matters. In many cases, it directly affects defects and local material properties. Sometimes it matters more than the thermal history itself.

Recent experiments show that diffusion zones formed during solidification can be measured and compared with numerical results [2]. Because of this, diffusion-controlled cases are often used as reference problems. Similar ideas appear in studies where solute distribution is rebuilt from experimental data and discussed using the basic solidification theory [3].

In numerical models, phase change is usually described on a fixed grid. The solid-liquid interface is not tracked directly. Latent heat is included using an enthalpy method or an effective heat capacity. One of the first and most common approaches was proposed by Voller and Prakash [4]. Later, Nedjar [5] developed finite-element methods based on enthalpy that can handle nonlinear phase-change problems. Similar methods were also used in other problems with layered or mixed materials and time-dependent response [6–8].

When alloys are considered, the problem becomes harder. Phase change and solute transport are linked and influence each other. Early analytical models of solute redistribution in mushy alloys are still useful today, especially as reference solutions [9]. More recent work uses numerical methods such as phase-field models, which describe diffusion and interface motion in one framework [10, 11]. Studies of multicomponent alloys show that different transport mechanisms affect segregation and solidification speed [12]. Finite-element multiscale models have also been used to study chemical segregation during steel solidification when extra transport effects are included [13]. In industrial applications, results from numerical simulations are commonly used to analyse segregation in continuous casting processes [14].

In this work, only diffusion-dominated solidification is considered. Fluid flow is not included. This choice allows the effects of diffusive solute transport and phase change to be studied in a clear way. Without convection, the interpretation of source terms and transport coefficients is simpler. For this reason, the global solute balance is used as a main control quantity and is checked during the simulations to ensure numerical consistency.

2. Mathematical model

The solidification process is considered in a two-dimensional square domain $\Omega \subset \mathbb{R}^2$, representing a simplified casting region. The model is restricted to diffusion-dominated transport. Fluid flow is neglected and the velocity field is assumed to be identically zero. As a consequence, the mathematical description is limited to heat conduction with phase change and solute diffusion coupled through segregation effects.

The boundary $\Gamma = \partial\Omega$ is divided into two disjoint parts. The left boundary Γ_D is subjected to cooling by a prescribed temperature (Dirichlet condition), while the remaining boundaries Γ_N are thermally insulated (zero Neumann condition). Under these assumptions, the solidification front initiates at the cooled boundary and propagates from left to right across the domain (Fig. 1).

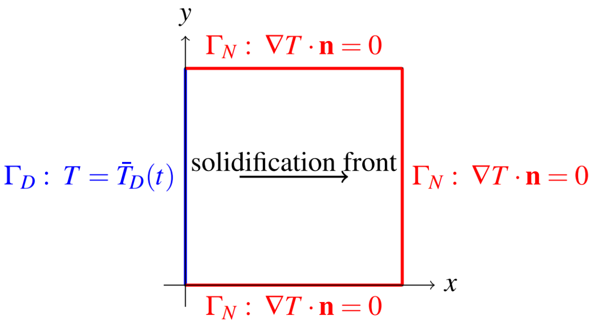

Fig. 1. Computational domain Ω and boundary conditions. The left boundary Γ_D is subject to a prescribed temperature (Dirichlet condition), while the remaining boundaries Γ_N are thermally insulated. The solidification front propagates from left to right

2.1. Phase description

The local liquid fraction f_l is defined as a piecewise-linear function of temperature between the solidus temperature T_s and the liquidus temperature T_l:

$$f_l(T) = \begin{cases} 0 & T \le T_s, \\ \dfrac{T - T_s}{T_l - T_s} & T_s < T < T_l, \\ 1 & T \ge T_l. \end{cases} \tag{1}$$

Its temperature derivative, required in the effective heat-capacity formulation, is given by:

$$\frac{df_l}{dT} = \begin{cases} 0 & T \le T_s \text{ or } T \ge T_l, \\ \dfrac{1}{T_l - T_s} & T_s < T < T_l. \end{cases} \tag{2}$$

2.2. Governing equations

The transient heat-conduction equation with phase-dependent material properties is written as:

$$\rho\, c_{\text{eff}}(T)\,\frac{\partial T}{\partial t} = \nabla \cdot (\lambda(T)\nabla T) \qquad \text{in } \Omega \times (0, t_{\text{end}}], \tag{3}$$

where the effective heat capacity incorporates the latent heat of solidification:

$$c_{\text{eff}}(T) = f_l(T)\,c_l + \big(1 - f_l(T)\big)\,c_s + L\,\frac{df_l}{dT}. \tag{4}$$

The thermal conductivity is interpolated according to the local phase state:

$$\lambda(T) = f_l(T)\,\lambda_l + \big(1 - f_l(T)\big)\,\lambda_s. \tag{5}$$

Let C_l denote the solute mass fraction in the liquid phase. In the absence of convection, solute transport is governed by diffusion with a phase-dependent diffusivity and a source term accounting for redistribution during the evolution of the liquid fraction. To ensure consistency with the diagnostic mixture quantity (8), the transient term is weighted by the factor $[k + f_l(1-k)]$:

$$\big[k + f_l(T)(1-k)\big]\,\frac{\partial C_l}{\partial t} = \nabla\cdot\left(D_{\text{eff}}(T)\,\nabla C_l\right) - (1-k)\,C_l\,\frac{\partial f_l}{\partial t} \qquad \text{in } \Omega\times(0,t_{\text{end}}], \tag{6}$$

where the effective diffusivity is defined as

$$D_{\text{eff}}(T) = f_l(T)\,D_l + \big(1 - f_l(T)\big)\,D_s, \tag{7}$$

For diagnostic purposes, a phase-mixture solute quantity is evaluated a posteriori from the local equilibrium relation $C_s^{eq} = kC_l$ as:

$$C_{\text{mix}} = f_l C_l + (1-f_l)\,C_s^{eq} = \big[k + f_l(1-k)\big]\,C_l. \tag{8}$$

2.3. Initial and boundary conditions

At the initial time $t = 0$, the temperature and solute fields are prescribed:

$$T(\mathbf{x},0) = T_0(\mathbf{x}), \qquad C_l(\mathbf{x},0) = C_{l,0}(\mathbf{x}) \qquad \text{in } \Omega. \tag{9}$$

On the cooled boundary Γ_D a Dirichlet condition is imposed:

$$T(\mathbf{x},t) = \bar{T}_D(t) \qquad \text{on } \Gamma_D\times(0,t_{\text{end}}], \tag{10}$$

while the remaining boundaries are thermally insulated:

$$-\lambda(T)\,\nabla T\cdot\mathbf{n} = 0 \qquad \text{on } \Gamma_N\times(0,t_{\text{end}}], \tag{11}$$

For the solute field, impermeable boundaries are assumed on the entire boundary:

$$-D_{\text{eff}}(T)\,\nabla C_l\cdot\mathbf{n} = 0 \qquad \text{on } \Gamma\times(0,t_{\text{end}}]. \tag{12}$$

where the symbols are defined as follows: T – temperature [K], t – time [s], $\mathbf{x}$ – spatial coordinates [m], f_l – liquid fraction [$-$], T_s, T_l – solidus and liquidus temperatures [K], ρ – density [kg m^{-3}], c_s, c_l – specific heat capacity [J kg^{-1} K^{-1}], c_{eff} – effective heat capacity [J kg^{-1} K^{-1}], L – latent heat [J kg^{-1}], λ_s, λ_l – thermal conductivity [W m^{-1} K^{-1}], C_l – solute mass fraction in the liquid phase [$-$], C_s^{eq} – equilibrium solute mass fraction in the solid phase [$-$], C_{mix} – phase-mixture solute quantity [$-$], D_l, D_s – solute diffusivity in liquid/solid [m^2 s^{-1}], D_{eff} – effective diffusivity [m^2 s^{-1}], k – partition coefficient [$-$], $\mathbf{n}$ – outward unit normal [$-$].

3. Numerical model

The governing equations (3) and (6) are solved by the finite element method on a conforming triangulation of Ω. Since the present study addresses a diffusion-dominated regime, the velocity field is set to $\mathbf{u} \equiv \mathbf{0}$ and the discretization reduces to transient diffusion with locally phase-dependent coefficients.

3.1. Spatial discretization and weak form

Let $\{N_i\}_{i=1}^{N}$ denote the standard continuous, piecewise-linear basis functions associated with the mesh nodes. The temperature and solute fields are approximated as:

$$T_h(\mathbf{x},t) = \sum_{j=1}^{N} N_j(\mathbf{x})\, T_j(t), \qquad C_{l,h}(\mathbf{x},t) = \sum_{j=1}^{N} N_j(\mathbf{x})\, C_{l,j}(t). \tag{13}$$

Applying the Galerkin method with test functions $w = N_i$ yields the semi-discrete forms. For the heat equation, one obtains:

$$\int_\Omega \rho\, c_{\text{eff}}(T_h) N_i \frac{\partial T_h}{\partial t}\, d\Omega + \int_\Omega \lambda(T_h) \nabla N_i \cdot \nabla T_h \, d\Omega = 0, \tag{14}$$

and for the solute equation (consistent with (6)):

$$\int_\Omega \left[k + f_l(T_h)(1-k)\right] N_i \frac{\partial C_{l,h}}{\partial t}\, d\Omega + \int_\Omega D_{\text{eff}}(T_h) \nabla N_i \cdot \nabla C_{l,h} \, d\Omega =$$

$$= -\int_\Omega (1-k)\, C_{l,h} N_i \frac{\partial f_l(T_h)}{\partial t}\, d\Omega. \tag{15}$$

Essential (Dirichlet) boundary conditions for temperature are imposed by direct substitution of the prescribed nodal values on Γ_D, which gives rise to the load vector $\mathbf{b}_T^{n+1}$ in the discrete system.

3.2. Time integration and algebraic systems

Time discretization is performed using a semi-implicit backward Euler scheme, where phase-dependent coefficients are evaluated using previously available fields. Denoting by $\mathbf{T}^n$ and $\mathbf{C}_l^n$ the vectors of nodal values at t^n, and $\Delta t = t^{n+1} - t^n$, the fully discrete systems read:

$$\Big[\mathbf{M}_T + \Delta t\,\mathbf{K}_T\Big]\mathbf{T}^{n+1} = \mathbf{M}_T\,\mathbf{T}^n + \Delta t\,\mathbf{b}_T^{n+1}, \tag{16}$$

$$\Big[\mathbf{M}_{C_l} + \Delta t\,\mathbf{K}_{C_l}\Big]\mathbf{C}_l^{n+1} = \mathbf{M}_{C_l}\,\mathbf{C}_l^n + \Delta t\,\mathbf{b}_{C_l}^{n+1}. \tag{17}$$

Here, $\mathbf{M}_T$ is the (temperature-dependent) heat-capacity matrix with entries:

$$\big(\mathbf{M}_T\big)_{ij} = \int_\Omega \rho\, c_{\mathrm{eff}}(T_h^n)\, N_i N_j\, d\Omega, \tag{18}$$

while $\mathbf{K}_T$ is the thermal conductivity matrix:

$$\big(\mathbf{K}_T\big)_{ij} = \int_\Omega \lambda(T_h^n)\,\nabla N_i \cdot \nabla N_j\, d\Omega. \tag{19}$$

Analogously, the solute mass matrix $\mathbf{M}_{C_l}(T_h^n)$ is weighted by the factor $[k + f_l(T_h^n)(1-k)]$:

$$\big(\mathbf{M}_{C_l}\big)_{ij} = \int_\Omega \big[k + f_l(T_h^n)(1-k)\big]\, N_i N_j\, d\Omega, \tag{20}$$

and $\mathbf{K}_{C_l}(T_h^n)$ is the diffusion matrix for solute:

$$\big(\mathbf{K}_{C_l}\big)_{ij} = \int_\Omega D_{\mathrm{eff}}(T_h^n)\,\nabla N_i \cdot \nabla N_j\, d\Omega. \tag{21}$$

At each time step the liquid fraction is updated from (1) using the current temperature field. The time derivative in (6) is approximated by a backward difference:

$$\left.\frac{\partial f_l}{\partial t}\right|^{n+1} \approx \frac{f_l^{n+1} - f_l^n}{\Delta t}, \tag{22}$$

and the segregation source term in the solute equation is evaluated using $C_{l,h}^n$ and $\partial f_l/\partial t|^{n+1}$.

The vectors $\mathbf{b}_T^{n+1}$ and $\mathbf{b}_{C_l}^{n+1}$ account for boundary conditions and for the segregation source term, respectively. In particular:

$$\big(\mathbf{b}_{C_l}^{n+1}\big)_i = -\int_\Omega (1-k)\, N_i\, C_{l,h}^n \left.\frac{\partial f_l}{\partial t}\right|^{n+1} d\Omega. \tag{23}$$

where the segregation source term is assembled using the previous-time-level $C_{l,h}^n$, within the adopted operator-splitting strategy, which may induce a short initial transient in the global solute balance.

3.3. Monitoring of global solute balance

To verify numerical consistency, the global solute balance is monitored during the simulation by integrating the phase-mixture solute quantity (8) over the domain. Using a nodal quadrature (lumped mass weights M_i), the diagnostic quantity is computed as:

$$\mathscr{B}_{\text{mix}}(t^n) = \sum_{i=1}^{N} C^n_{\text{mix},i} M_i, \qquad M_i \approx \int_{\Omega} N_i \, d\Omega, \tag{24}$$

where $C^n_{\text{mix},i}$ is evaluated a posteriori from (8) using the nodal values of C_l and f_l at time level t^n. In the absence of inflow/outflow for solute (condition (12)), $\mathscr{B}_{\text{mix}}$ should remain constant up to numerical errors.

4. Example of calculations

The numerical simulations were carried out using an in-house finite element solver developed by the authors. The code was written to handle coupled diffusion and solidification with phase change. Time integration scheme is used. The solver also allows convective effects to be switched off, which makes it possible to study purely diffusion-controlled cases. The test case is a two-dimensional problem. The domain is a square with side length $a = 0.1$ m. It is discretized using an unstructured finite element mesh with $N_n = 53,225$ nodes. The whole domain represents a single material region and is treated as an interior subdomain. To focus only on diffusion effects, fluid flow is not taken into account. No external velocity field is applied. As a result, the evolution of temperature and solute concentration is driven only by diffusion and source terms related to phase change. The simulated material is a medium-carbon steel with a carbon content of about 0.45 %. Phase-dependent thermophysical properties used in the calculations are listed in Table 1. Constant values of solidus and liquidus temperatures are assumed. This choice is consistent with the diffusion-controlled solidification model adopted in this study.

Table 1. Material properties used in the numerical simulation

Property	Solid phase	Liquid phase
Density ρ [kg m^{-3}]	7850	
Thermal conductivity λ [W m^{-1} K^{-1}]	35	25
Specific heat c [J kg^{-1} K^{-1}]	650	820
Solute diffusivity D [m^2 s^{-1}]	0	$3.0 \cdot 10^{-9}$
Solidus temperature T_s [K]	1693	
Liquidus temperature T_l [K]	1733	
Latent heat L [J kg^{-1}]	$2.50 \cdot 10^5$	
Partition coefficient k [−]	0.3	

The initial temperature is equal to $T(\mathbf{x},0) = 1800$ K, i.e. above the liquidus temperature. A fixed temperature boundary condition $T = 600$ K is imposed on the left boundary, while the remaining boundaries are thermally insulated. The initial solute mass fraction is equal to $C_l(\mathbf{x},0) = 0.0045$, and zero solute flux is prescribed on the domain boundary. Time integration is carried out using a semi-implicit scheme with a constant time step $\Delta t = 0.01$ s. Scalar quantities are recorded every `prstep`=100 time steps, while full field data are exported every `sstep`=1000 steps.

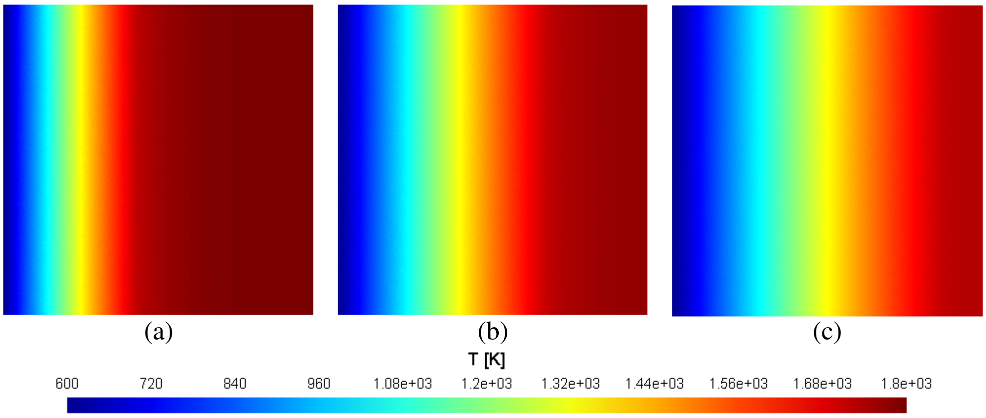
(a) (b) (c)

Fig. 2. Temperature distribution at different times during solidification: a) $t = 100$ s, b) $t = 250$ s, c) $t = 400$ s

Figure 2 shows how the temperature field changes during diffusion-dominated solidification. At $t = 100$ s (Fig. 2a), a strong temperature gradient appears close to the cooled boundary. This is caused by intensive heat removal through conduction. At $t = 250$ s (Fig. 2b), the thermal front moves deeper into the domain. The temperature field stays smooth and changes in a simple, monotonic way, which confirms that convective effects are not present. At $t = 400$ s (Fig. 2c), the gradient zone becomes wider as the solidification front continues to move forward. The temperature evolves in a continuous and stable manner, which indicates a numerically consistent solution of the transient heat-transfer problem.

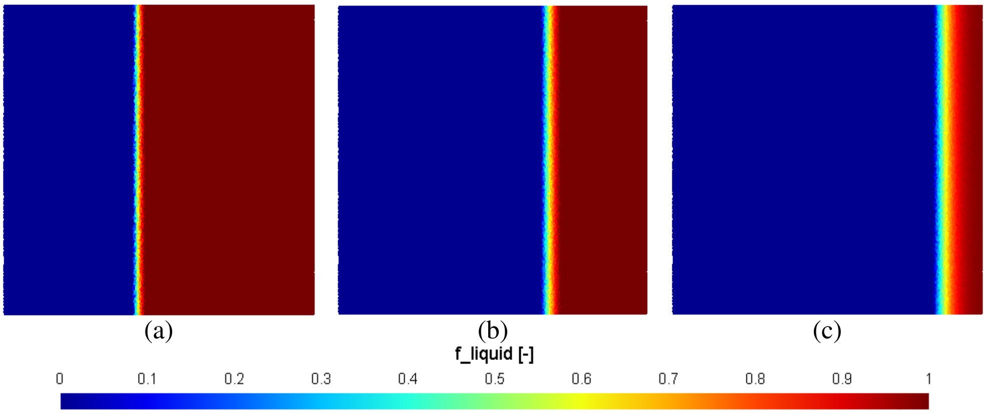
(a) (b) (c)

Fig. 3. Liquid fraction f_l at different times during solidification: a) $t = 100$ s, b) $t = 250$ s, c) $t = 400$ s

Figure 3 presents the changes of liquid fraction during diffusion-dominated solidification. At $t = 100$ s (Fig. 3a), a clear boundary between liquid and solid appears near the cooled surface. The transition is sharp and easy to identify. At $t = 250$ s

(Fig. 3b), the solid region grows and the phase boundary moves deeper into the domain. The interface is still well defined. At $t = 400$ s (Fig. 3c), most of the domain is already solid. The remaining liquid is limited to a thin region close to the moving solidification front.

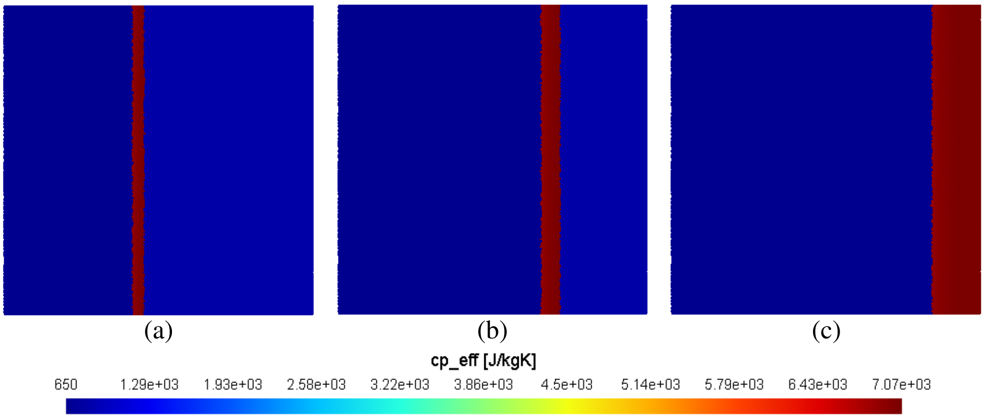
(a) (b) (c)

Fig. 4. Spatial distribution of the effective heat capacity c_{eff}, resulting from phase change at different times: a) $t = 100$ s, b) $t = 250$ s, c) $t = 400$ s

In Figure 4 the effective heat capacity distribution during solidification is presented. At $t = 100$ s (Fig. 4a), a narrow region with higher values of c_{eff} can be seen. This region corresponds to the mushy zone, where phase change takes place. As time passes, the situation changes. At $t = 250$ s and $t = 400$ s (Fig. 4b and Fig. 4c), this region moves deeper into the domain. It also becomes wider. This shows that the zone where phase change occurs grows with time.

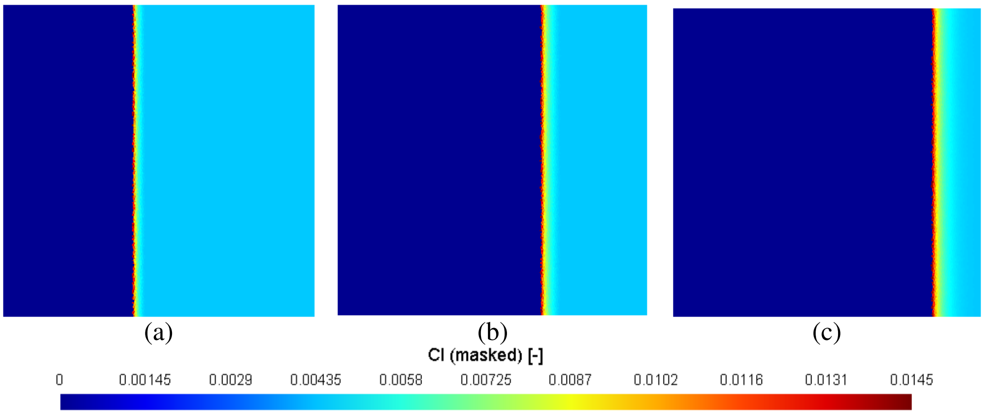
(a) (b) (c)

Fig. 5. Solute mass fraction in the liquid phase C_l at different times: a) $t = 100$ s, b) $t = 250$ s, c) $t = 400$ s

Figures 5-7 show how solute redistributes during diffusion-dominated solidification. In Figure 5 a clear peak of solute concentration appears in the liquid phase at the moving solidification front. The liquid solute mass fraction reaches about $C_l \approx 0.0145$, while the initial value was $C_{l,0} = 0.0045$. For the assumed partition coefficient $k = 0.3$, this result is expected. According to the simple equilibrium relation $C_l \approx C_{l,0}/k$, the solute concentration in the liquid near the interface should increase by about a factor of three. The value observed in the simulation follows this trend. The corresponding solid-phase concentration, $C_s^{eq} = kC_l$, is shown in Figure 6. As expected, it is limited to a narrow region close to the solidification front. Away from the front, this quantity quickly drops. Even though a strong local solute exchange occurs between the liquid and solid phases, the mixed-phase solute concentration C_{mix} remains smooth in space, as shown in Figure 7. This indicates that the segregation source term mainly redistributes solute locally. At the same time, the total solute content is preserved, which confirms global solute conservation in the model.

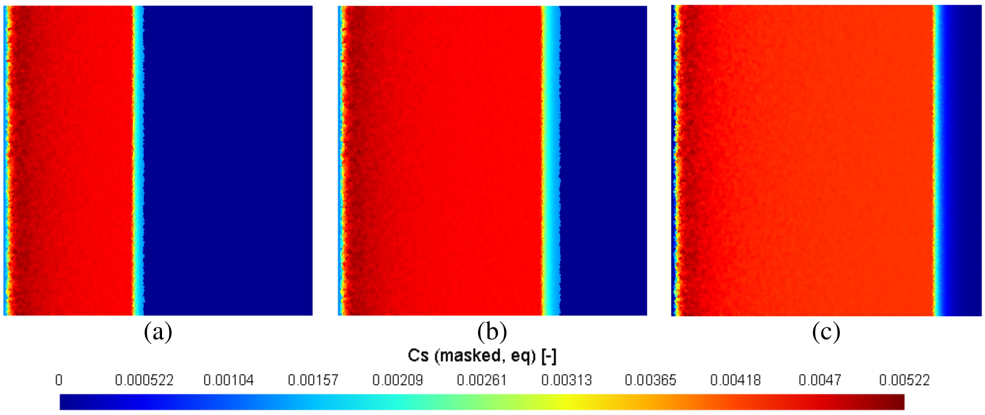
(a) (b) (c)

Fig. 6. Equilibrium solute mass fraction in the solid phase $C_s^{eq} = kC_l$, evaluated a posteriori at different times: a) $t = 100$ s, b) $t = 250$ s, c) $t = 400$ s

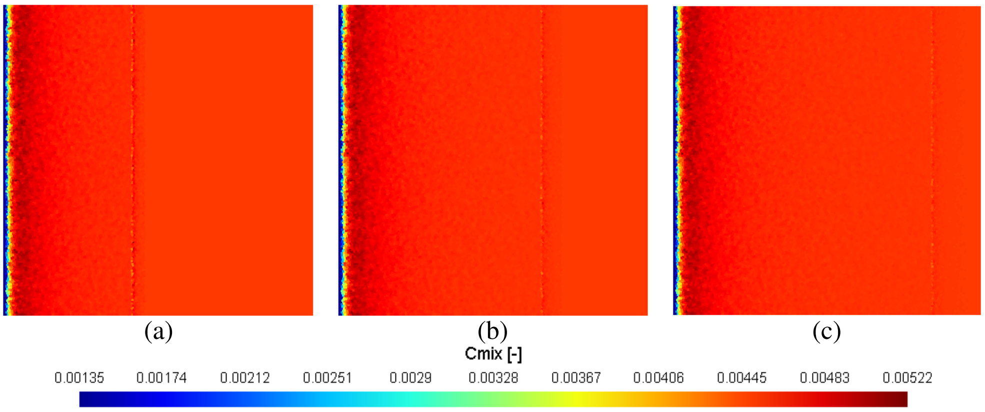
(a) (b) (c)

Fig. 7. Phase-mixture solute quantity C_{mix} at different times: a) $t = 100$ s, b) $t = 250$ s, c) $t = 400$ s

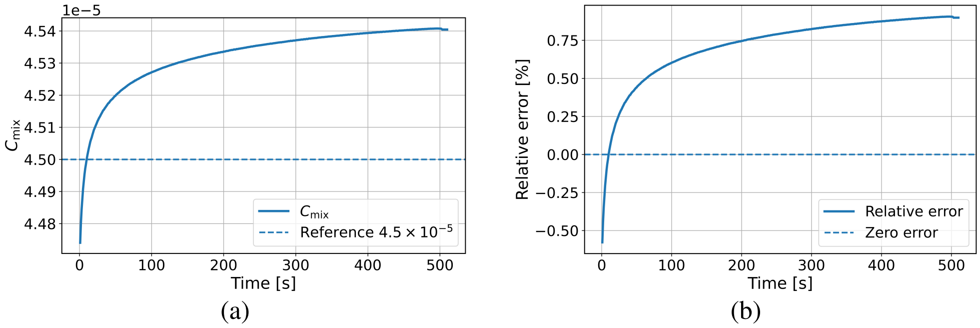

Fig. 8. Global phase-mixture solute balance during solidification: a) time evolution of the integral quantity C_{mix}, b) relative error of the global C_{mix} balance with respect to the initial reference value

Figure 8 shows how the global solute balance of the phase mixture changes during the simulation. It is also used to check if the numerical solution is consistent. As shown in Figure 8a, the integral value of the phase–mixture solute quantity C_{mix} stays close to its initial value during the whole solidification process. Only a small deviation appears at the beginning. This happens when phase change starts and the segregation source term becomes active. After this early stage, the global balance becomes almost constant. This means that solute redistribution mainly takes place locally and does not affect the overall balance. The relative error is shown in Figure 8b. It stays below 1% during the entire simulation time. After a short initial transient, the error changes slowly. No oscillations or long-term drift are observed. This confirms that the numerical scheme is stable and that the solute transport equation is consistent with the diagnostic phase-mixture quantity.

5. Conclusions

A diffusion-based solidification model with phase-dependent material properties was developed and solved using the finite element method. Convective transport was not included. This was done on purpose, in order to focus only on diffusion and phase change and to obtain a clear reference case for solute redistribution. The effective heat-capacity approach allows stable simulation of temperature and phase evolution without tracking the solid-liquid interface explicitly. The results show physically reasonable movement of the solidification front and solute enrichment in the mushy zone. The weighted solute transport equation, which includes a source term related to phase change, is consistent with the phase-mixture quantity C_{mix}. Even though strong solute exchange occurs locally between phases, the global C_{mix} balance is preserved with only a small relative error. This confirms the numerical stability of the model. The proposed formulation can therefore serve as a simple and reliable reference for testing and comparing more advanced solidification models.

References

[1] Suliga, M., Szota, P., & Mróz, S. (2017). Simulation and measurement of temperature in high speed drawing process of steel wires. *Computer Methods in Materials Science*, *17*(1), 69-75. DOI: 10.7494/cmms.2017.1.0577.

[2] Jia, Y., Shang, X., Yuan, L., Yang, G., & Shu, D. (2024). A quantitative study of the solute diffusion zone during solidification of Al-Cu alloys via in-situ synchrotron X-radiography and numerical simulation. *Materials & Design*, *247*, 113398. DOI: 10.1016/j.matdes.2024.113398.

[3] Dépinoy, S., Sennour, M., Ferhat, L., & Colin, C. (2021). Experimental determination of solute redistribution behavior during solidification of additively manufactured 316L. *Scripta Materialia*, *194*, 113663. DOI: 10.1016/j.scriptamat.2020.113663.

[4] Voller, V.R., & Prakash, C. (1987). A fixed grid numerical modelling methodology for mushy region phase-change problems. *International Journal of Heat and Mass Transfer*, *30*(8), 1709-1719. DOI: 10.1016/0017-9310(87)90317-6.

[5] Nedjar, B. (2002). An enthalpy-based finite element method for nonlinear heat problems involving phase change. *Computers & Structures*, *80*(1), 9-21. DOI: 10.1016/S0045-7949(01)00165-1

[6] Pozorska, J. (2018). Numerical modelling of sandwich panels with a non-continuous soft core. *MATEC Web of Conferences*, 157, 06007. DOI: 10.1051/matecconf/201815706007.

[7] Pozorska, J., Pozorski, Z., & Janik, L. (2017). Numerical simulations of structural behavior of sandwich panels subjected to concentrated static loads. *Journal of Applied Mathematics and Computational Mechanics*, *16*(2), 113-121. DOI: 10.17512/jamcm.2017.2.09.

[8] Ablaoui, E.M., Pozorska, J., Pozorski, Z., Roszkowski, P., & Malendowski, M. (2025). Numerical modelling of sandwich panels subjected to fire conditions. *Journal of Applied Mathematics and Computational Mechanics*, *24*(3), 5-17. DOI: 10.17512/jamcm.2025.3.01.

[9] Clyne, T.W., & Kurz, W. (1981). Solute redistribution during solidification with rapid solid-state diffusion. *Metallurgical Transactions A*, *12*, 965-971. DOI: 10.1007/BF02643477.

[10] Zhang, A., Guo, Z., Jiang, B., Xiong, S., & Pan, F. (2023). Numerical solution to phase-field model of solidification: A review. *Computational Materials Science*, *228*, 112366. DOI: 10.1016/j.commatsci.2023.112366.

[11] Al Azad, A.R., Cardiff, P., & Browne, D.J. (2023). Development and numerical testing of a model of equiaxed alloy solidification using a phase field formulation. *Metals*, *13*(12), 1916. DOI: 10.3390/met13121916.

[12] Wang, Y., Tourret, D., & Abdeljawad, F. (2024). A computational study of solidification kinetics in multicomponent alloys. *Computational Materials Science*, *244*, 113161. DOI: 10.1016/j.commatsci.2024.113161.

[13] Nguyen, T.-T.-M., Gandin, C.-A., Combeau, H., Založnik, M., & Bellet, M. (2018). Finite element multi-scale modeling of chemical segregation in steel solidification. *Metallurgical and Materials Transactions A*, *49*(2), 1725-1748. DOI: 10.1007/s11661-018-4496-4.

[14] Chen, H., Long, M., Chen, D., Liu, T., & Duan, H. (2018). Numerical study on solute distribution and centerline segregation in continuous casting slab. *International Journal of Heat and Mass Transfer*, *126*, 843-853. DOI: 10.1016/j.ijheatmasstransfer.2018.05.081.